Novel and Enhanced Optoelectronic Performances of Multilayer MoS_2–WS_2 Heterostructure Transistors

Nengjie Huo, Jun Kang, Zhongming Wei, Shu-Shen Li, Jingbo Li, and Su-Huai Wei**

Van der Waals heterostructures designed by assembling isolated two-dimensional (2D) crystals have emerged as a new class of artificial materials with interesting and unusual physical properties. Here, the multilayer MoS_2–WS_2 heterostructures with different configurations are reported and their optoelectronic properties are studied. It is shown that the new heterostructured material possesses new functionalities and superior electrical and optoelectronic properties that far exceed the one for their constituents, MoS_2 or WS_2. The vertical transistor exhibits a novel rectifying and bipolar behavior, and can also act as photovoltaic cell and self-driven photodetector with photoswitching ratio exceeding 10^3. The planar device also exhibits high field-effect ON/OFF ratio (>10^5), high electron mobility of 65 cm^2/Vs, and high photoresponsivity of 1.42 A/W compared to that in isolated multilayer MoS_2 or WS_2 nanoflake transistors. The results suggest that formation of MoS_2–WS_2 heterostructures could significantly enhance the performance of optoelectronic devices, thus open up possibilities for future nanoelectronic, photovoltaic, and optoelectronic applications.

1. Introduction

Graphene as a two-dimensional (2D) material has attracted extensive attentions recently due to its unusual physicochemical properties[1–4] and its great potentials in various technological applications such as nanoelectronics and optoelectronics.[5–8] However, the zero bandgap of graphene has limited its applications. As alternatives, new research interests have emerged focusing on other 2D materials such as transition metal sulfides (TMDs) (WS_2, MoS_2, etc.), which possess sizable band gap around 1–3 eV and display advantageous optoelectronic properties.[9,10] For example, the field-effect transistors based on monolayer or few-layer MoS_2 have been reported to exhibit an excellent on/off ratio (~10^8) and room-temperature mobility of >200 cm^2/Vs, and the layered WS_2 has also been reported to exhibit 10^5 room temperature modulation and bipolar behavior.[11,12] For photodetection, the layered TMDs based photodetectors have been demonstrated with very high responsivity and fast photoresponse.[13–15]

In parallel with the study of the single layer graphene-like materials, Van der Waals heterostructures and the corresponding devices fabricated by stacking different 2D crystals on top of each other have also been gaining much attention recently. These systems have revealed some novel properties and new phenomena that could trigger new revolution in architecture design of heterostructures for integrated optoelectronic applications. For example, the graphene heterostructures with 2D h-BN or MoS_2 layers acting as vertical transport barrier are fabricated and exhibit room-temperature switching ratio of 50 and 10 000, respectively.[16] Following the success, the vertical integration of multi-heterostructures of graphene and MoS_2 are reported for the fabrication of a new generation of vertical field-effect transistors[17] (VFETs) with an on-off ratio >10^3 and a high current density of up to 5000 A/cm^2. The vertically stacked heterostructures of graphene and MoS_2 are also demonstrated to display remarkable multiple optoelectronic functionality, including highly sensitive photodetection and gate-tunable persistent photoconductivity,[18] gate-tunable photocurrent generation with a maximum internal quantum efficiency up to 85%, and huge capacity of information storage with a factor of 10^4 difference between memory states and erase states.[19,20] Moreover, the VFETs based on the graphene-WS_2 heterostructures are also fabricated with unprecedented current modulation exceeding 10^6 at room temperature.[21] These results suggest that the stacked multi-heterostructures of layered materials could open up new opportunities in future nanoelectronic devices with large-scale integration. Indeed, there are large number of 2D materials that can be exfoliated with micromechanical cleavage method and combined together to create various and tailored heterostructures.

N. Huo, J. Kang, Prof. S.-S. Li, Prof. J. Li
Country State Key Laboratory for
Superlattices and Microstructures
Institute of Semiconductors
Chinese Academy of Sciences
P.O. Box 912
Beijing 100083, China
E-mail: jbli@semi.ac.cn
Dr. Z. Wei
Nano-Science Center & Department of Chemistry
University of Copenhagen
Universitetsparken 5
DK-2100, Copenhagen Ø, Denmark
Dr. S.-H. Wei
National Renewable Energy Laboratory
1617 Cole Boulevard, Golden, CO 80401, USA
E-mail: suhuai.wei@nrel.gov

DOI: 10.1002/adfm.201401504

Here, we describe vertical field-effect transistors based on multilayer MoS_2 and WS_2 heterostructure, which exhibit novel rectifying and bipolar behavior with much improved switching on/off ratio of 10^5 or larger. The designed heterostructure also exhibits unusual optoelectronic property, which can be used for high efficiency self-driven photodetectors with maximum photo-switching ratio of 10^3 due to the presence of a built-in potential in the heterostructure. The MoS_2–WS_2 heterostructure planar transistors are also demonstrated to possess better optoelectronic performances than the isolated multilayer MoS_2 or WS_2 nanoflake transistors, including the improved field-effect ON/OFF ratio (>10^5), high electron mobility of 65 cm^2/Vs, and high photoresponsivity of 1.42 A/W.

2. Results and Discussion

As typical 2D layered semiconductors, MoS_2 and WS_2 possess similar crystalline structure and lattice constants,[22] so the interface between MoS_2 and WS_2 could be strain free with minimal structural defects. Each single plane of MS_2 (M = Mo or W) comprises a trilayer composed of a molybdenum or tungsten layer sandwiched between two sulfur layers in a trigonal prismatic coordination (**Figure 1**a). The layered MoS_2 and WS_2 are binded by weak Van der Waals force, and first-principle calculation reveals that the band offset between MoS_2 and WS_2 presents type-II characteristics, namely, both the CBM and VBM of WS_2 are higher in energy than those of MoS_2 as shown from the calculated band structures (Figure 1b) and band alignment (Figure 1c), which is in agreement with previous reports.[23,24] The vertically stacked MoS_2–WS_2 heterostructures are fabricated with dry transfer procedure.[21,25] Briefly, the multilayer MoS_2 nanoflakes are exfoliated onto the SiO_2/Si substrates with micromechanical cleavage method. The multilayer WS_2 nanoflakes are then transferred onto another substrate to overlap with the MoS_2 nanoflakes. Then, the Au electrodes serving as source and drain are deposited by "gold-wire mask moving" method.[26,27] Two types of architectures are designed for the devices, which are vertical and planar transistors as shown in Figure 1d,e, respectively. In the vertical architecture, the source

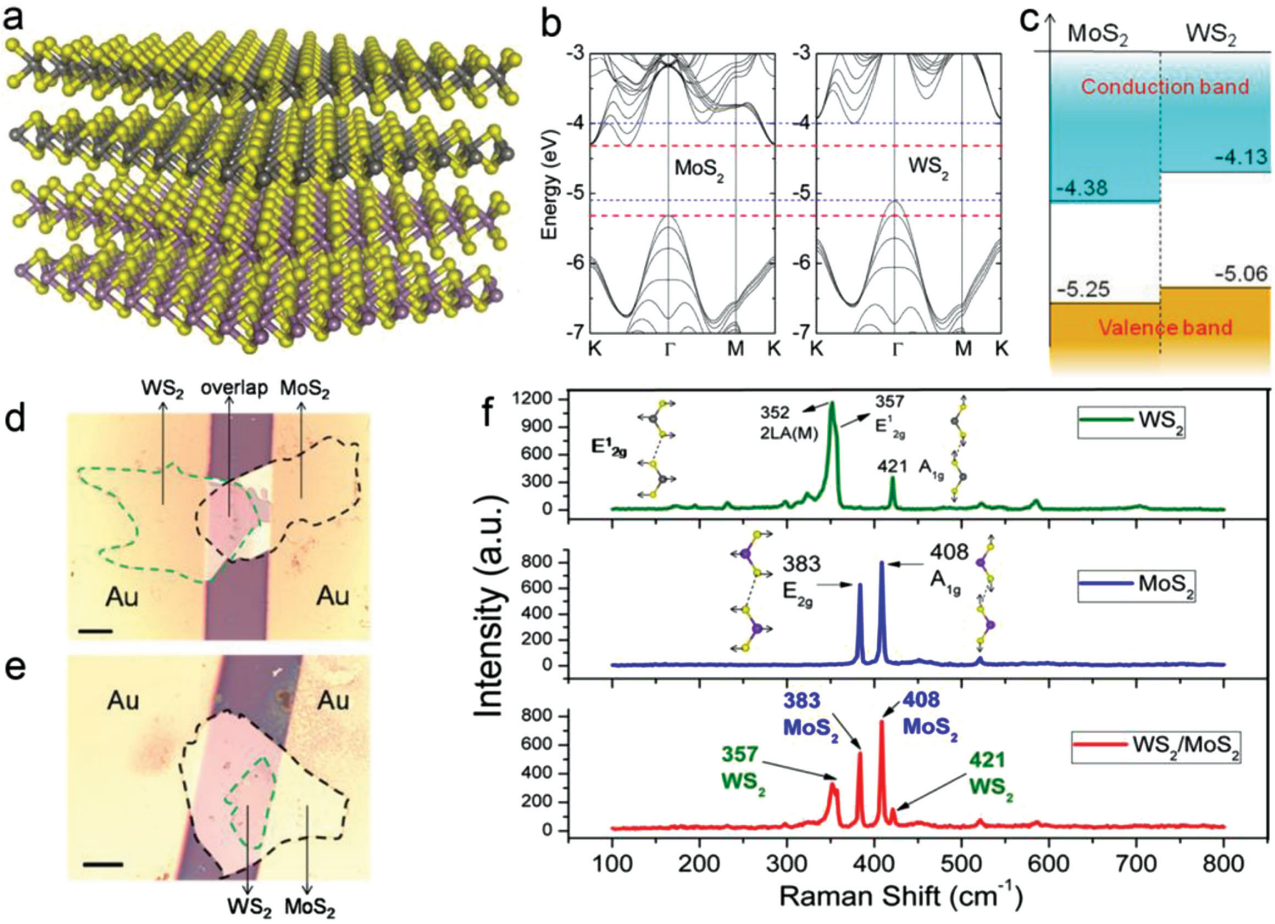

Figure 1. a) Three-dimensional schematic plot of a typical WS_2 and MoS_2 structure with the sulfur atoms in yellow, tungsten atoms in gray and the molybdenum atoms in purple. b,c) The calculated band structure (b) and band alignment (c) for multilayer MoS_2 and WS_2 nanoflakes, presenting type-II structure. The vacuum level is taken as zero reference (eV). d) The optical microscope images of the stacked multilayer MoS_2–WS_2 heterostructure transistors in vertical architecture. The scale bar is 10 μm. e) Same as (d) but in planar architecture. f) Room-temperature Raman spectrum from the multilayer WS_2 and MoS_2 nanoflakes, and the MoS_2–WS_2 heterostructures, using the 532 nm laser. The inset is a schematic illustration of the atomic displacements for the in-plane phonon mode $E^1_{2g}(\Gamma)$ and the out-of-plane phonon mode $A_{1g}(\Gamma)$, for two adjacent layers of WS_2 or MoS_2, the dashed line represents the weak inter-layer van der Waals interaction.

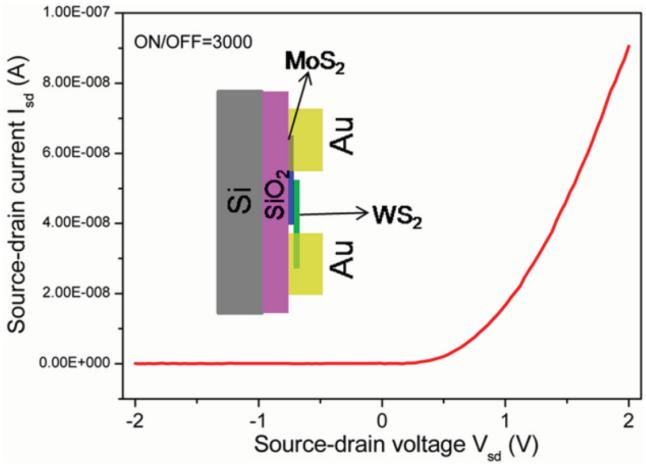

Figure 2. Current–voltage characteristics of vertical transistor based on the MoS_2–WS_2 heterostructures. The inset shows the schematic diagram of the device.

and drain electrodes are connected to the MoS_2 and WS_2 flakes, respectively, whereas in the planar architecture, both source and drain electrodes are connected to the MoS_2 flakes. More details of the fabrication procedures will be described in the Experimental Section.

The first-order Raman spectra of both the multilayer WS_2 and MoS_2 nanoflakes show two optical phonon modes at the Brillouin zone center [$E^1_{2g}(\Gamma)$ and $A_{1g}(\Gamma)$]. $E^1_{2g}(\Gamma)$ is an in-plane optical mode, while $A_{1g}(\Gamma)$ corresponds to out-of-plane vibrations of the sulfur atoms (inset of Figure 1f). Figure 1f shows the Raman spectra of exfoliated multilayer WS_2 and MoS_2 nanoflakes as well as the stacked WS_2–MoS_2 heterostructures. The first-order Raman peaks are identified at 357 and 421 cm^{-1} for WS_2, and 383 and 408 cm^{-1} for MoS_2, which are attributed to the $E^1_{2g}(\Gamma)$ and $A_{1g}(\Gamma)$ modes, respectively. The Raman peaks of MoS_2–WS_2 heterostructures contains the typical vibration modes of both MoS_2 and WS_2, indicating the formation of heterostructures.

Figure 2 shows the *I*–*V* characteristics of vertical transistor based on MoS_2–WS_2 heterostructures, which exhibits obvious rectifying behavior with forward-to-reverse bias current ratios of 10^3. The observed linear *I*–*V* characteristics (Figure S1, Supporting Information) suggest Au makes Ohmic contacts to the isolated MoS_2 and WS_2 nanoflakes. As shown in Figure 1b,c, the MoS_2 and WS_2 nanoflakes have a type-II band alignment. In order to achieve balance between electron potential when they are binded together to form heterostructures, some electrons are transferred from WS_2 into MoS_2, resulting in the existence of a built-in potential in the interface. When a positive bias is applied, the built-in potential decreases and the conducting electrons can more easily drift from the WS_2 side to MoS_2 resulting in the On-state of the device. On the contrary, the barrier height increases and less electrons can across the contact barrier under a negative source bias, leading to a much smaller reverse current.

It is interesting that the vertical transistor exhibits not only rectifying but also bipolar properties. **Figure 3**a,b shows the transfer and output characteristics of the device under positive source–drain with bias voltage V_{sd} = 5 V, exhibiting strong n-type behavior with an on-off ratio reaching almost 10^5, which could be further improved by increasing the gate voltage V_g or V_{sd}, whereas under negative V_{sd} (–10 V), the device shows p-type behavior with an on-off ratio in the order of 10 (Figure 3c,d). The transistors based on the isolated multilayer MoS_2 and WS_2 nanoflakes were also fabricated (Figure S2a,b, Supporting Information). The transfer and output characteristics plotted in Figure S3a–d,S4 (Supporting Information) show that both the multilayer MoS_2 and WS_2 nanoflakes exhibit n-type behavior under either positive or negative V_{sd} with on-off ratio of only 200 and 10 times, respectively. The abnormal gate modulation for the vertical MoS_2–WS_2 heterostructures can be explained by using the band diagrams (Figure 3e-3h), depicting the cases under positive and negative V_{sd}, respectively. The band shape and MoS_2–WS_2 barrier height can be effectively modulated by an external voltage V_g applied through the silicon back-gate electrode.[16,17,19] With negative V_g, the MoS_2 and WS_2 are heavily hole-doped near the SiO_2 substrate and the hole doping in MoS_2 is larger, resulting in the downward band slope across the entire stack from MoS_2 to WS_2 (Figure 3g). On the contrary, with positive V_g, the electrons concentration in both MoS_2 and WS_2 increase near the SiO_2 dielectric substrate and shift the Fermi level upwards, forming an upward band slope (Figure 3h). In our device, under the positive V_{sd}, the electrons migrate from WS_2 to MoS_2 and the upward band slope from the applied positive V_g can facilitate the current drift process, presenting the On-state, whereas applying negative V_g will make the device switch off due to the formation of reverse barrier attributed to the downward band slope. In the case of the negative V_{sd}, only few electrons in MoS_2 can across the barrier into the WS_2 with positive V_g, whereas more electrons can drift and tunnel into WS_2 with downward band slope when negative V_g is applied, resulting in the increased source–drain current I_{sd}. As a result, the vertical MoS_2–WS_2 heterostructure devices exhibit n-type conducting behavior under On-state, whereas p-type conducting behavior under the Off-state.

Besides the vertical device, we also fabricated the planar transistor based on the MoS_2–WS_2 heterostructures, in which the source–drain Au electrodes are located at two sides of MoS_2 nanoflakes overlapped by WS_2 nanoflakes at the top. The schematic diagram of the planar device is shown in the inset of **Figure 4**a. From the observed near linear *I*–*V* characteristics (Figure S5, Supporting Information) and the transfer and output characteristics under different V_{sd} (Figure S6, Supporting Information), we see that the planar transistor exhibits no rectifying and bipolar properties. Figure 4 shows the transfer and output characteristics of the planar transistor that exhibits strong n-type behavior with ON/OFF ratio exceeding 10^5. Using the band diagram (Figure 3g,h), we can easily understand the improved field-effect ON/OFF ratio. Under the positive gate voltage V_g, some electrons in WS_2 could transfer into the MoS_2, increasing the electron concentration in MoS_2, thus increasing its On-state current. When a negative V_g is applied, the induced band slope facilitates the depletion of electrons in MoS_2, leading to reduced Off-state current. As a result, the ON/OFF ratio is substantially improved in the planar transistor based on MoS_2–WS_2 heterostructures compared to that in separate multilayer MoS_2 nanoflake based transistor.

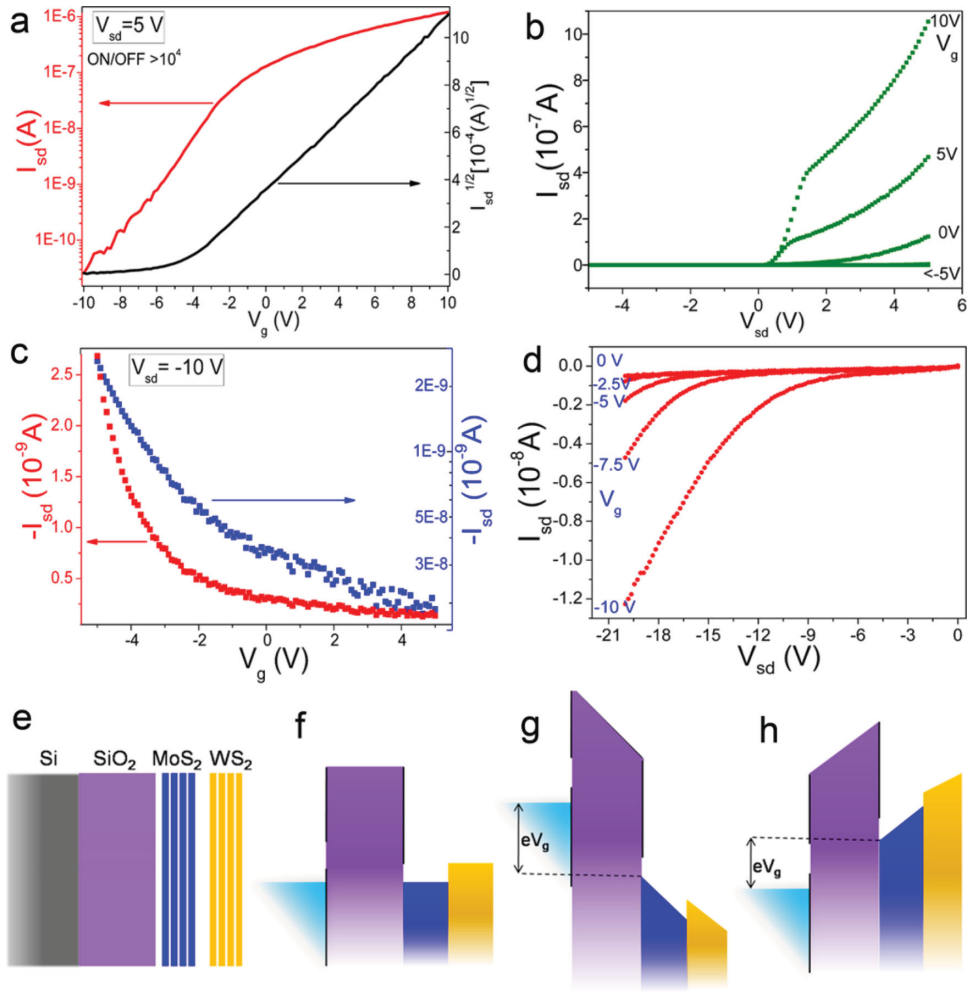

Figure 3. a) Transfer and b) output characteristics of the vertical transistors based on MoS_2–WS_2 heterostructures in the case of On-state. c) Transfer and d) output characteristics under the Off-state. e) Schematic plot of the transistor in vertical architecture. f) Band diagram corresponding to no V_g. g) Band diagram under negative V_g, showing downward energy slop from MoS_2 to WS_2. h) Band diagram under positive V_g, showing upward energy slop from MoS_2 to WS_2.

The mobility (μ) can be obtained from the equation $\mu = \frac{\partial I_{sd}}{\partial V_g}\left(\frac{L}{WC_i V_{sd}}\right)$, where L is the channel length, W is the channel width, and C_i is the gate capacitance between the channel and the silicon back gate per unit area, which can be given by equation $C_i = \varepsilon_0\varepsilon_r/d$, ε_0 (8.85×10^{-12} F/m) is vacuum dielectric constant, and ε_r (3.9) and d (300 nm) are dielectric constant and thickness of SiO_2, respectively. **Table 1** lists the calculated field-effect electron mobility and ON/OFF ratio of multilayer MoS_2, WS_2 nanoflakes and MoS_2–WS_2 heterostructures. We find that electron mobility is significantly improved in the MoS_2–WS_2 heterostructures, especially for the planar MoS_2–WS_2 heterostructure transistors, which exhibit electron mobilities as high as 65 cm^2/Vs, that is, much higher than that of our isolated multilayer MoS_2 or WS_2 nanoflakes, and previous reported monolayer WS_2 (μ = 0.01 cm^2/Vs) and the widely studied monolayer MoS_2 (μ = 0.1–10 cm^2/Vs) fabricated without high-κ dielectrics.[11,28,29] The novel and enhanced performance, including improved ON/OFF ratio and mobility, rectifying, and bipolar properties

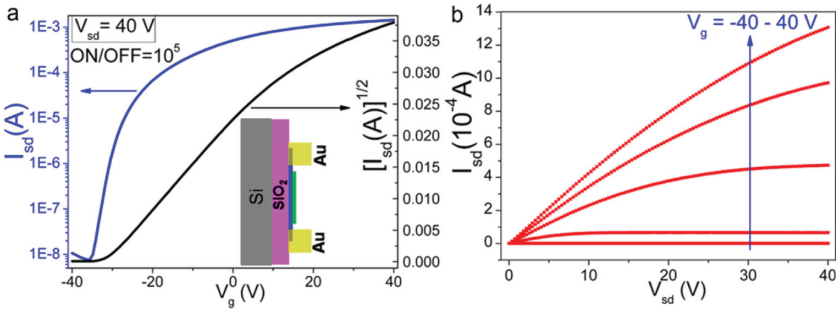

Figure 4. a) Transfer characteristics of the planar transistor based on the MoS_2–WS_2 heterostructures. The inset shows a schematic diagram of the planar device. b) Output characteristics of the planar device.

Table 1. Calculated field-effect performance parameters including electron mobility μ and ON/OFF ratio of the transistors based on the multilayer MoS_2, WS_2 nanoflakes and MoS_2–WS_2 heterostructures with different architecture.

Parameters	MoS_2	WS_2	Vertical MoS_2–WS_2	Planar MoS_2–WS_2
μ	20	3.5	14	65
ON/OFF ratio	200	10	$>10^4$	10^5

suggest that the MoS_2–WS_2 heterostructures have huge potential in future nanoelectronics applications.

In addition, the photoresponsive properties of the vertical and planar transistors based on the MoS_2–WS_2 heterostructures were examined using a 633 nm laser at room temperature. **Figure 5**a shows the time dependence of the photocurrent I_{sd} at different positive source–drain voltage V_{sd}. The source–drain current I_{sd} can change between high and low states quickly and repetitively with photo-switching on/off ratio of about 5 times. With increased V_{sd}, the photocurrent can be significantly increased. Moreover, in the case of negative V_{sd}, namely under the Off-state of the device, the photo-switching on/off ratio can reach as high as 10^3 times due to the very low dark current, and the photocurrent is less sensitive with increased negative V_{sd} (Figure 5b). Figure 5c shows the I–V curves under dark and upon light illumination with different light power density, depicting the formation of short-circuit current I_{sc} and open-circuit voltage V_{oc} upon light illumination, which increase with the light power, indicating an excellent photovoltaic property. The maximum V_{oc} can reach 0.25 V. Another important phenomenon we observe is that the vertical transistors based on MoS_2–WS_2 heterostructures can also perform as a self-driven photodetector without applying source–drain bias V_{sd} (Figure 5d), and the photocurrent can change repetitively and rapidly with light switching on/off.

For the vertical transistor based on the MoS_2–WS_2 heterostructures, when a positive V_{sd} is applied (On-state), not only the photo-excited electron-hole pairs but also the electrical carriers can contribute to the photocurrent I_{sd}. However, under negative V_{sd} (Off-state), the electrical carriers are much less and the photo-excited carriers dominate, so with the increased V_{sd}, the increments of current are more obvious in On-state than that in Off-state. Moreover, under the Off-state, both the very low dark current and dominated photocurrent result in the high photo-switching on/off ratio. Under the condition of open circuit, the photo-excited electron-hole pairs can be separated under the built-in potential, and the electrons and holes can accumulate in MoS_2 and WS_2, respectively. Along with the increase of light power, the amounts of the accumulated electrons and holes increase, resulting in the enhanced built-in potential (inset of Figure 5c). When the heterostructures are short circuited, the electrons and holes can be driven by the built-in potential, producing the short-circuit current, which contributes to the realization of photovoltaic cell and self-driven photodetector.

Figure 5e,f shows the photocurrent as a function of light density under an excitation wavelength of 633 nm. The photocurrent shows a strong dependence on light intensity and the experimental data is fitted by a power equation $I_{ph} = aP^{\alpha}$, where a is a scaling constant, and α is an exponent. In our device with zero or negative bias, the photocurrent displays

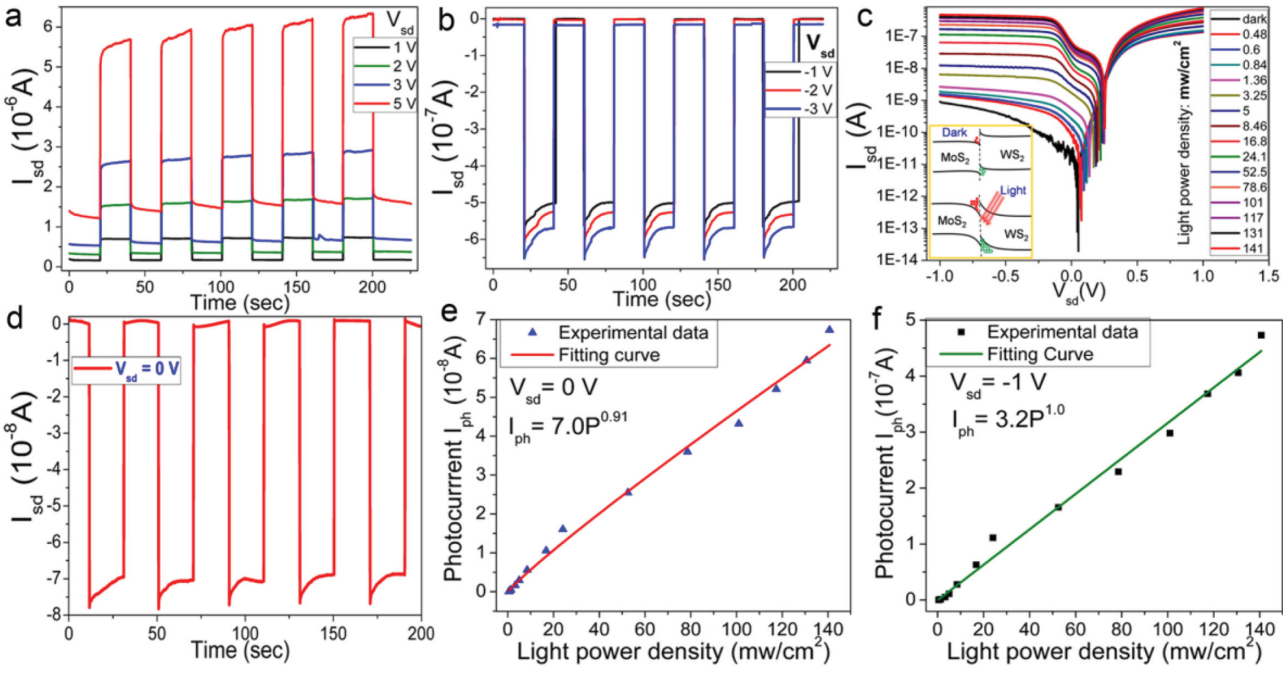

Figure 5. a) Time dependence of source–drain current I_{sd} of the vertical transistor based on the MoS_2–WS_2 heterostructures during the light (633 nm, 141 mW/cm^2) switching on/off under the positive source–drain voltage V_{sd} from 1 to 5 V and b) under the negative V_{sd} from −1 to −3 V. c) I_{sd}–V_{sd} characteristics of the vertical device with increasing incident light power density. The inset is the corresponding band diagram under dark and light illumination. d) Time dependence of I_{sd} with zero V_{sd}, indicating the realization of self-driven photodetector. e,f) Photocurrent (defined as $I_{ph} = I_{light} - I_{dark}$) as function of light power density with V_{sd} of 0 V and −1 V, respectively.

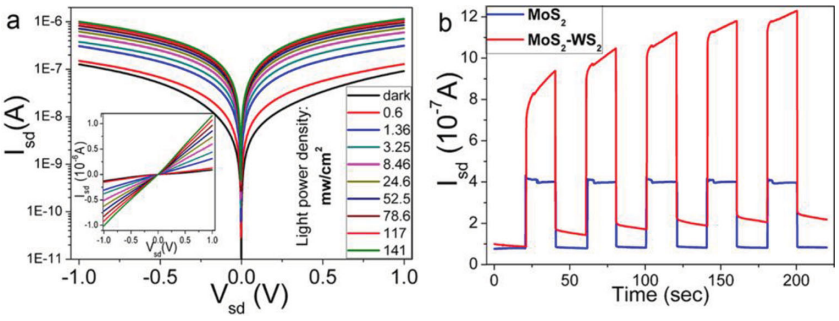

Figure 6. a) I_{sd}–V_{sd} characteristics of the planar transistor based on MoS_2–WS_2 heterostructures under different light illumination density. The inset is the corresponding data plotted in linear scale. b) Time dependence of I_{sd} of MoS_2 and MoS_2–WS_2 heterostructure planar transistors during the light (633 nm, 141 mW/cm^2) switching on/off.

a power dependence of ≈0.91 or ≈1.00 (i.e., $I_{ph} = 7.0P^{0.91}$ or $I_{ph} = 3.2P^{1.00}$), indicating a superior photocurrent capability and a high efficiency of photo-generated charge carriers from the absorbed photons.

As for the planar transistors based on the MoS_2–WS_2 heterostructures, the photovoltaic properties are not observed. **Figure 6**a shows the *I–V* curves under dark and light illumination with different light density, revealing symmetric and zero I_{sc} and V_{oc}. The results can be attributed to the in-plane migration of conducting carriers in the MoS_2 nanoflakes and the absence of built-in potential in the planar device. We also found the prolonged response time and improved photocurrent in the device compared to the isolated MoS_2 nanoflakes (Figure 6b), which must be related to the overlapped WS_2 nanoflakes on top of MoS_2. We know that the WS_2 nanoflakes exhibit excellent photosensitivity (Figure S7, Supporting Information). Although the electrical carriers do not pass through the WS_2 nanoflakes, the photo-generated electrons in WS_2 can transfer into the MoS_2 under the energy gradient at the interfaces[30,31] and contribute to its conductivity. The rise and fall time can increase to thousands of seconds (Figure S8, Supporting Information), indicating the slow charge transfer process between the MoS_2 and WS_2 during the light switching on or off.

Photoresponsivity R_λ and external quantum efficiency EQE are critical parameters for evaluating the quality of photodetectors. Large value of R_λ and EQE corresponds to high light-sensitivity. R_λ and EQE can be expressed as $R_\lambda = I_{ph}/PS$ and $EQE = hcR_\lambda/e\lambda$, where I_{ph} is the photo-excited current; P is the light power intensity; S is the effective illumination area; h is Planck's constant; c is the velocity of light; e is the electron charge; and λ is the excitation wavelength. The calculated results under the same incident light power (141 mW/cm^2) and source–drain bias of 1 V are listed in Table 2. The R_λ and EQE for the MoS_2–WS_2 heterostructures are improved, especially, the maximum value for the planar device can reach 1.42 A/W and 278%, respectively, which are three orders of magnitude larger than the photodetectors reported for graphene or monolayer MoS_2.[6,32] All the remarkable performance parameters of the MoS_2–WS_2 heterostructure based photodetectors, including photo-switching on/off ratio, light dependence of exponent α and photoresponsivity R_λ demonstrate that the MoS_2–WS_2 heterostructures can also be used in highly sensitive and self-driven photodetectors and fast photoelectric switches.

Table 2. Calculated photoresponsive performance parameters including photoresponsivity R_λ and external quantum efficiency EQE of the transistors based on the multilayer MoS_2, WS_2 nanoflakes and MoS_2–WS_2 heterostructures with different architecture.

Parameters	MoS_2	WS_2	Vertical MoS_2–WS_2	Planar MoS_2–WS_2
R_λ [A/W]	0.44	0.62	0.76	1.42
EQE [%]	86%	122%	149%	278%

3. Conclusion

In summary, the vertical and planar transistors based on the multilayer MoS_2–WS_2 nanoflakes heterostructures are fabricated with dry transfer and "gold-wire mask moving" method. Novel and excellent field-effect and photosensitivity are observed in the MoS_2–WS_2 heterostructures with new functionalities and superior electrical and optoelectronic properties that far exceed the one for their constituents, MoS_2 or WS_2. The vertical device exhibits a rectifying property with forward-to-reverse bias current ratios of 10^3 and a bipolar behavior which has an n-type behavior with an ON/OFF ratio more than 10^4 under positive V_{sd} and a p-type behavior with an ON/OFF ratio of 10 times under negative V_{sd}. The observed behavior can be attributed to the type-II band alignment between MoS_2 and WS_2 and the band slope induced by the gate voltage. The multilayer MoS_2–WS_2 nanoflake vertical heterostructures can also act as photovoltaic cell and self-driven photodetector due to the existence of built-in potential. Under the Off-state, the photo-switching on/off ratio can be increased to over 10^3 times. The planar device also exhibits high field-effect ON/OFF ratio (> 10^5), and high electron mobility of 65 cm^2/Vs, as well as high photoresponsivity of 1.42 A/W compared to that in isolated multilayer MoS_2 and WS_2 nanoflakes based transistors. All these novel and remarkable field-effect and photoresponsive performances suggest that the MoS_2–WS_2 heterostructures possess huge potential in future nanoelectronics, optoelectronic, and photovoltaic applications.

4. Experimental Section

Fabrication of Multilayer MoS_2–WS_2 Heterostructures: The multilayer MoS_2–WS_2 heterostructures were fabricated with dry transfer method. Firstly, the multilayer MoS_2 and WS_2 nanoflakes were exfoliated onto two pieces of SiO_2/Si (300 nm SiO_2) substrates respectively from the MoS_2 and WS_2 crystals (2D semiconductors.com) with micromechanical cleavage approach. Secondly, the polymethyl methacrylate (PMMA) liquid was spin coated on the substrate with WS_2 nanoflakes with rotating speed of 4000 r/s. After annealing with 150 °C for 30 min, the substrate with PMMA film was soaked into the 2 M NaOH solution. Then, the PMMA film with WS_2 nanoflakes was floated and transferred onto another substrate to overlap with the MoS_2 nanoflakes. At last, the PMMA was dissolved by acetone and the stacked MoS_2–WS_2 heterostructures were achieved.

Fabrication of Vertical and Planar Transistors: The transistors based on the MoS_2, WS_2 nanoflakes and MoS_2–WS_2 heterostructures were fabricated with "gold-wire mask moving" technique. A micrometer gold-wire serving as a mask was fixed tightly on the top surface of the materials, and then a pair of Au electrodes was deposited onto the substrate by thermal evaporation. To avoid the scattering of metallic atoms onto the side-face of SiO_2/Si substrates, the sides of the substrate were covered with tinfoil, moreover, the distance between the thermal evaporation boat and the sample was increased to 15 cm and the deposition rate was controlled at around 1 Å/s in order to minimize the heat influence. Finally, by slightly removing the Au wire mask and tinfoil, the Au electrodes were fabricated and a micrometer size gap was produced between the two electrodes. For the vertical transistors based on the MoS_2–WS_2 heterostructures, the source Au electrode was deposited on the WS_2 nanoflakes and the drain Au electrode was on MoS_2 nanoflakes. For the planar transistors, both the source and drain electrodes were deposited on the MoS_2 nanoflakes with WS_2 nanoflakes on top.

Measurements and Characterization: The images of the multilayer MoS_2, WS_2 nanoflakes and MoS_2–WS_2 heterostructures based transistors were detected with Optical microscope. The Raman spectra were measured from 100–800 cm^{-1} using the 532 nm wavelength of a He-Ne laser. Field-effect properties were measured with Transistor test system (Agilent-B2902). Photoelectrical experiments were performed with a CHI660D electrochemical workstation in a conventional three-electrode electrochemical cell.

Supporting Information

Supporting Information is available from the Wiley Online Library or from the author.

Acknowledgements

This work was supported by the National Natural Science Foundation of China under Grant No.91233120 and the National Basic Research Program of China (2011CB921901). The work of S.-H.W. is supported by the U.S. Department of Energy under Contract No. DE-AC36–08GO28308.

Received: May 9, 2014
Published online: September 5, 2014

[1] A. K. Geim, *Science* **2009**, *324*, 1530.
[2] P. Avouris, Z. Chen, V. Perebeinos, *Nat. Nanotechnol.* **2007**, *2*, 605.
[3] C. N. R. Rao, A. Sood, K. S. Subrahmanyam, A. Govindaraj, *Angew. Chem. Int. Ed.* **2009**, *48*, 7752.
[4] F. Schwierz, *Nat. Nanotechnol.* **2010**, *5*, 487.
[5] M. Liu, X. Yin, E. Ulin-Avila, B. Geng, T. Zentgraf, L. Ju, F. Wang, X. Zhang, *Nature* **2011**, *474*, 64.
[6] F. Xia, T. Mueller, Y. Lin, A. Valdes-Garcia, P. Avouris, *Nat. Nanotechnol.* **2009**, *4*, 839.
[7] D. C. Elias, R. V. Gorbachev, A. S. Mayorov, S. V. Morozov, A. A. Zhukov, P. Blake, L. A. Ponomarenko, I. V. Grigorieva, K. S. Novoselov, F. Guinea, A. K. Geim, *Nat. Phys.* **2011**, *7*, 701.
[8] A. K. Geim, K. S. Novoselov, *Nat. Mater.* **2007**, *6*, 183.
[9] J. A. Wilson, A. D. Yoffe, *Adv. Phys.* **1969**, *18*, 193.
[10] A. D. Yoffe, *Annu. Rev. Mater. Sci.* **1973**, *3*, 147.
[11] B. Radisavljevic, A. Radenovic, J. Brivio, V. Giacometti, A. Kis, *Nat. Nanotechnol.* **2011**, *6*, 147.
[12] W. S. Hwang, M. Remskar, R. Yan, V. Protasenko, K. Tahy, S. D. Chae, P. Zhao, A. Konar, H. Xing, A. Seabaugh, D. Jena, *Appl. Phys. Lett.* **2012**, *101*, 013107.
[13] D. S. Tsai, K. K. Liu, D. H. Lien, M. L. Tsai, C. F. Kang, C. A. Lin, L. J. Li, J. H. He, *ACS Nano* **2013**, *7*, 3905.
[14] O. Lopez-Sanchez, D. Lembke, M. Kayci, A. Radenovic, A. Kis, *Nat. Nanotechnol.* **2013**, *8*, 497.
[15] W. Zhang, J.-K. Huang, C.-H. Chen, Y.-H. Chang, Y.-J. Cheng, L.-J. Li, *Adv. Mater.* **2013**, *25*, 3456.
[16] L. Britnell, R. V. Gorbachev, R. Jalil, B. D. Belle, F. Schedin, A. Mishchenko, T. Georgiou, M. I. Katsnelson, L. Eaves, S. V. Morozov, N. M. R. Peres, J. Leist, A. K. Geim, K. S. Novoselov, L. A. Ponomarenko, *Science* **2012**, *335*, 947.
[17] W. J. Yu, Z. Li, H. Zhou, Y. Chen, Y. Wang, Y. Huang, X. Duan, *Nat. Mater.* **2013**, *12*, 246.
[18] K. Roy, M. Padmanabhan, S. Goswami, T. P. Sai, G. Ramalingam, S. Raghavan, A. Ghosh, *Nat. Nanotechnol.* **2013**, *8*, 826.
[19] W. J. Yu, Y. Liu, H. Zhou, A. Yin, Z. Li, Y. Huang, X. Duan, *Nat. Nanotechnol.* **2013**, *8*, 952.
[20] S. Bertolazzi, D. Krasnozhon, A. Kis, *ACS Nano* **2013**, *7*, 3246.
[21] T. Georgiou, R. Jalil, B. D. Belle, L. Britnell, R. V. Gorbachev, S. V. Morozov, Y.-J. Kim, A. Gholinia, S. J. Haigh, O. Makarovsky, L. Eaves, L. A. Ponomarenko, A. K. Geim, K. S. Novoselov, A. Mishchenko, *Nat. Nanotechnol.* **2013**, *8*, 100.
[22] X. Su, R. Zhang, C. Guo, M. Guo, Z. Ren, *Phys. Chem. Chem. Phys.* **2014**, *16*, 1393.
[23] J. Kang, S. Tongay, J. Zhou, J. Li, J. Wu, *Appl. Phys. Lett.* **2013**, *102*, 012111.
[24] K. Kośmider, J. Fernández-Rossier, *Phys. Rev. B* **2013**, *87*, 075451.
[25] A. L. Elías, N. Perea-López, A. Castro-Beltrán, A. Berkdemir, R. Lv, S. Feng, A. D. Long, T. Hayashi, Y. A. Kim, M. Endo, H. R. Gutiérrez, N. R. Pradhan, L. Balicas, T. E. Mallouk, F. López-Urías, H. Terrones, M. Terrones, *ACS Nano* **2013**, *7*, 5235.
[26] Q. Tang, H. Li, M. He, W. Hu, C. Liu, K. Chen, C. Wang, Y. Liu, D. Zhu, *Adv. Mater.* **2006**, *18*, 65.
[27] Q. Tang, H. Li, Y. Liu, W. Hu, *J. Am. Chem. Soc.* **2006**, *128*, 14634.
[28] Y. H. Lee, L. Yu, H. Wang, W. Fang, X. Ling, Y. Shi, C. T. Lin, J. K. Huang, M. T. Chang, C. S. Chang, M. Dresselhaus, T. Palacios, L. J. Li, J. Kong, *Nano Lett.* **2013**, *13*, 1852.
[29] K. S. Novoselov, D. Jiang, F. Schedin, T. J. Booth, V. V. Khotkevich, S. V. Morozov, A. K. Geim, *Proc. Natl Acad. Sci. U.S.A.* **2005**, *102*, 10451.
[30] N. Huo, Q. Yue, J. Yang, S. Yang, J. Li, *ChemPhysChem* **2013**, *14*, 4069.
[31] J. Li, L. W. Wang, *Chem. Mater.* **2004**, *16*, 4012.
[32] Z. Yin, H. Li, L. Jiang, Y. Shi, Y. Sun, G. Lu, Q. Zhang, X. Chen, H. Zhang, *ACS Nano* **2012**, *6*, 74.